Green Chemistry

PAPER

View Article Online
View Journal | View Issue

Cite this: *Green Chem.*, 2024, **26**, 5988

Upcycling spent lithium-ion battery cathodes into cobalt-polyphenol networks by DES dissolution and solvent-induced crystallization†

Zeyu Wang,[a] Yu Chen,[b] Fengyi Zhou,[a] Rui Qin,[a] Yurun Tian,[a] Zhimin Xue[c] and Tiancheng Mu*[a]

The industrialization of the recycling of spent lithium-ion batteries presents promising opportunities and challenges. Herein, we developed a strategy of combining task-specific deep eutectic solvent (3,4,5-trihydroxybenzoic acid: choline chloride) dissolution and the following solvent-induced crystallization (SIC) for upcycling $LiCoO_2$ (LCO) battery cathodes into cobalt-polyphenol networks. It has been confirmed that protic solvents (ethylene glycol, methanol, ethanol, and H_2O) serve as effective inducing agents to achieve this strategy, playing a role in: (1) regulating the coordination environment of metal ions, initiating the self-assembly process with polyphenol anions and (2) provoking the precipitation of metal-polyphenol network particles (MPNPs) by altering the solubility. Comprehensive research indicated that when organic building blocks (phenolic acid, polyphenol compounds and their derivatives), Cl^-, and inducing agents concurrently exist in the system, one-step conversion from LCO to MPNPs could be achieved. A tandem scheme is proposed based on the research for upcycling LCO into MPNPs, which are applied widely in separation, purification and catalysis. Experiments on ternary electrode materials demonstrated the robust generalizability of our strategy. This work provides valuable insights for the industrialization of spent LCO battery recycling and its transformation into novel materials.

Received 29th February 2024,
Accepted 1st April 2024

DOI: 10.1039/d4gc01036a

rsc.li/greenchem

Introduction

In recent years, lithium-ion batteries (LIBs) have undergone diversification within the field of energy storage technology due to their remarkable advantages such as high energy density, longer cycle life, and wide operating temperature range.[1] They are widely applied in portable electronic devices, electric vehicles, medical equipment, and large-scale grid energy storage solutions.[2] Various types of LIBs employ distinct electrode materials. Current commercial cathodes employ materials such as $LiCoO_2$ (LCO), $LiNi_{0.8}Co_{0.15}Al_{0.05}O_2$ (NCA), $LiNi_{1/3}Co_{1/3}Mn_{1/3}O_2$ (NCM), and $LiFePO_4$ (LFP), alongside anodes such as graphite or $Li_4Ti_5O_{12}$.[3,4] Additionally, new electrode materials have been proposed to improve their performance. The expansion of lithium energy market inevitably leads to the generation of wastes due to long-time usage. Waste LIBs contain valuable materials, particularly cathodes composed of rare or strategic metals such as cobalt, nickel, and lithium. These materials exhibit higher concentrations and purities compared to natural ores, making them widely utilized as "urban mine" for extraction and separation of rare metals.[5] Pyrometallurgy and hydrometallurgy are prevalent treatment methods for waste LIBs;[6] however, they pose challenges related to environmental pollution and high energy consumption. In recent years, more environmentally sustainable solvent metallurgy methods have emerged.[7] Solvent metallurgy relies on eco-friendly solvents such as deep eutectic solvents (DESs),[5] which possess greater environmental compatibility than hydrometallurgy. DESs exhibit exceptionally low vapor pressure, broader electrochemical windows, and high thermal stability, positioning them as the leading candidates for future green solvent applications.[8]

The use of choline chloride-based DESs for the recycling of spent LIB cathode materials was initially proposed by Tran *et al.*[7] Density functional theory (DFT) calculations demonstrated that ethylene glycol plays a role in breaking the M–O bond at high temperatures, while Cl^- reacts with metal ions to form metal–chloride complexes.[9] More acidic DESs have been proposed based on lactic acid,[10] citric acid,[11] tartaric acid,[12] and malic acid.[13] Most of these systems exhibit excellent dissolution efficiency for electrode materials; however, there is

[a]*Department of Chemistry, Renmin University of China, Beijing 100872, P.R. China. E-mail: tcmu@ruc.edu.cn*
[b]*Department of Chemistry and Material Science, Langfang Normal University, Langfang 065000, Hebei, P.R. China. E-mail: yuchen@iccas.ac.cn*
[c]*Beijing Key Laboratory of Lignocellulosic Chemistry, Beijing Forestry University, Beijing 100083, P.R. China. E-mail: zmxue@bjfu.edu.cn*

†Electronic supplementary information (ESI) available. See DOI: https://doi.org/10.1039/d4gc01036a

still a lack of research on high recovery of metal ions. Solvent-induced crystallization (SIC) represents a distinctive approach for precipitating metal ions. Metal ions are converted into either crystalline or amorphous compounds by the inducing agents.[14] The SIC is primarily governed by factors such as solvent composition, the nature and quantity of inducing agents, and the characteristics of solutes. Due to current reliance on experimental findings, there exists considerable uncertainty in designing this process.

A metal-phenolic network (MPN) represents supramolecular coordination structures formed *via* the assembly of metal ions and polyphenolic ligands.[15] The presence of numerous metal ion binding sites on phenolic ligands results in the complex manifesting as an infinitely extended three-dimensional coordination network.[16] Nanoparticles with the structure of MPN can be obtained *via* the direct self-assembly of polyphenolic ligands and metal ions in aqueous solutions, obviating the use of primers or templates. Xu *et al.* have recently disclosed a catalog of polyphenol ligands suitable for the fabrication of metal-polyphenol network particles (MPNPs). These ligands can be directly assembled with metal ions in non-toxic aqueous solutions.[17] This serves as a reference for expanding the scope of SIC systems because designing DESs to produce high-molecular weight polymer particles composed of metal ions, such as MPNPs, is possible. Drawing from the synthesis of MOF (metal–organic framework) nanoparticles using "initiation-solvent",[18] these polymers may demonstrate limited solubility in both DESs and inducing agents, thereby achieving the separation and purification of metal ions.

In this work, we used 3,4,5-trihydroxybenzoic acid (gallic acid, abbreviated as GA), as a polyphenol ligand in the fabrication of MPNPs. We conducted the dissolution of $LiCoO_2$ using a task-specific GA-ChCl DES and the subsequent recovery of dissolved cobalt ions through conversion into MPNPs *via* SIC. The experimental results indicate that four conventional proton solvents possess the capability of facilitating the self-assembly process of cobalt ions with GA anions. We confirmed that the disparity in valence and coordination environments of metal ions in the center results in MPNPs with varying crystalline structures. Investigations revealed that efficient one-step conversion into cobalt-based MPNPs could be achieved when the organic building blocks, chloride salts, and inducing agents were concurrently present within the system. These findings hold a significant reference value for the industrial recovery of spent LCO batteries and its transformation into novel materials.

Results and discussion

Preparation and characterization of GA-based DESs

DESs were prepared by combining GA as the hydrogen bond donor (HBD) and ChCl as the hydrogen bond acceptor (HBA) in a molar ratio of 1 : 2 (Fig. 1a). The individual components, GA and ChCl, exhibit melting points of 251 °C and 302 °C, respectively. In the DES, the eutectic point decreases to approximately 76 ± 3 °C. Nuclear magnetic resonance (NMR) and Fourier-transform infrared (FT-IR) spectroscopy confirmed the presence of hydrogen bonds between GA and ChCl (Fig. S1, ESI†). Thermogravimetry (TG) analysis of the DES revealed a three-stage weight loss process (Fig. S2, ESI†). The DES exhibits stability within the temperature range of 80 °C–120 °C (reaction temperature range in this study). The reduction behaviour of DESs at different ratios was further investigated by cyclic voltammetry (CV) (Fig. S3, ESI†). Alterations in the reduction behaviour of the DES notably influenced its capacity to solubilize LCO.[19] The DES exhibits optimal reduction ability when the molar ratio of GA and ChCl was 1 : 2. Therefore, this DES was used in the subsequent experiments.

Assembly strategy and characterization of MPNPs

The scheme for the conversion of LCO to MPNPs is shown in Fig. 1b. The preparation of the DES was carried out at 90 °C, after which LCO was dissolved for complete leaching. Then EG was added and reacted, accompanied by a gradual color change from dark green to brown. This is due to the suspension and dispersion of MPNPs. The morphologies of GA, LCO, and MPNPs were characterized respectively. The MPNPs exhibit a dumbbell structure with a homogeneous morphology, approximately 2.2 μm in length and 0.9 μm in width under a SEM (Fig. 1d), which differs from GA and LCO (Fig. S4, ESI†). Additionally, nanoscale rod-shaped aggregates are present at both ends of the dumbbell. The FTIR spectrum illustrates that the molecular structure of GA is well preserved in the MPN (Fig. S5, ESI†). Energy-dispersive spectroscopy (EDS) demonstrates the elemental species and distribution in MPNPs (Fig. 1e and Fig. S6, ESI†). The presence of element N suggests that choline chloride is involved in forming coordination polymers. The even distribution of elements C, O, and Co suggests the formation of network structures based on coordination bonds, rather than core–shell structures composed of an organic polymer encapsulating the metal oxide.

Additionally, we explored other proton solvents such as H_2O, EtOH, and MeOH. Fig. 1c and Fig. S7† display the SEM images of MPNPs obtained using these solvents as inducers, respectively. MPNPs obtained from MeOH (Fig. 1c-i) exhibited an ellipsoidal structure with an average diameter of 600 nm, while particles from H_2O (Fig. 1c-ii) exhibited a spindle-like structure, resembling the morphology of GA-based MOF materials.[20] Sharp X-ray diffraction (XRD) patterns demonstrate the high crystallinity of MPNPs (Fig. 1f), because thermodynamically controlled processes at high temperatures facilitate the assembly of metal ions and polyphenols into crystalline products.[21] Four crystalline MPNPs exhibited structural similarities in pairs. Particles obtained from H_2O and EG display the most intense crystallographic diffraction peak at $2\theta = 11.39°$. However, when MeOH and EtOH are employed, it is observed at $2\theta = 44.08°$. The disparity in the crystalline structure of MPNPs may be associated with the valence state of cobalt ions (see details later). TG analysis further demonstrates the similarity in the thermal stability of the four crystalline

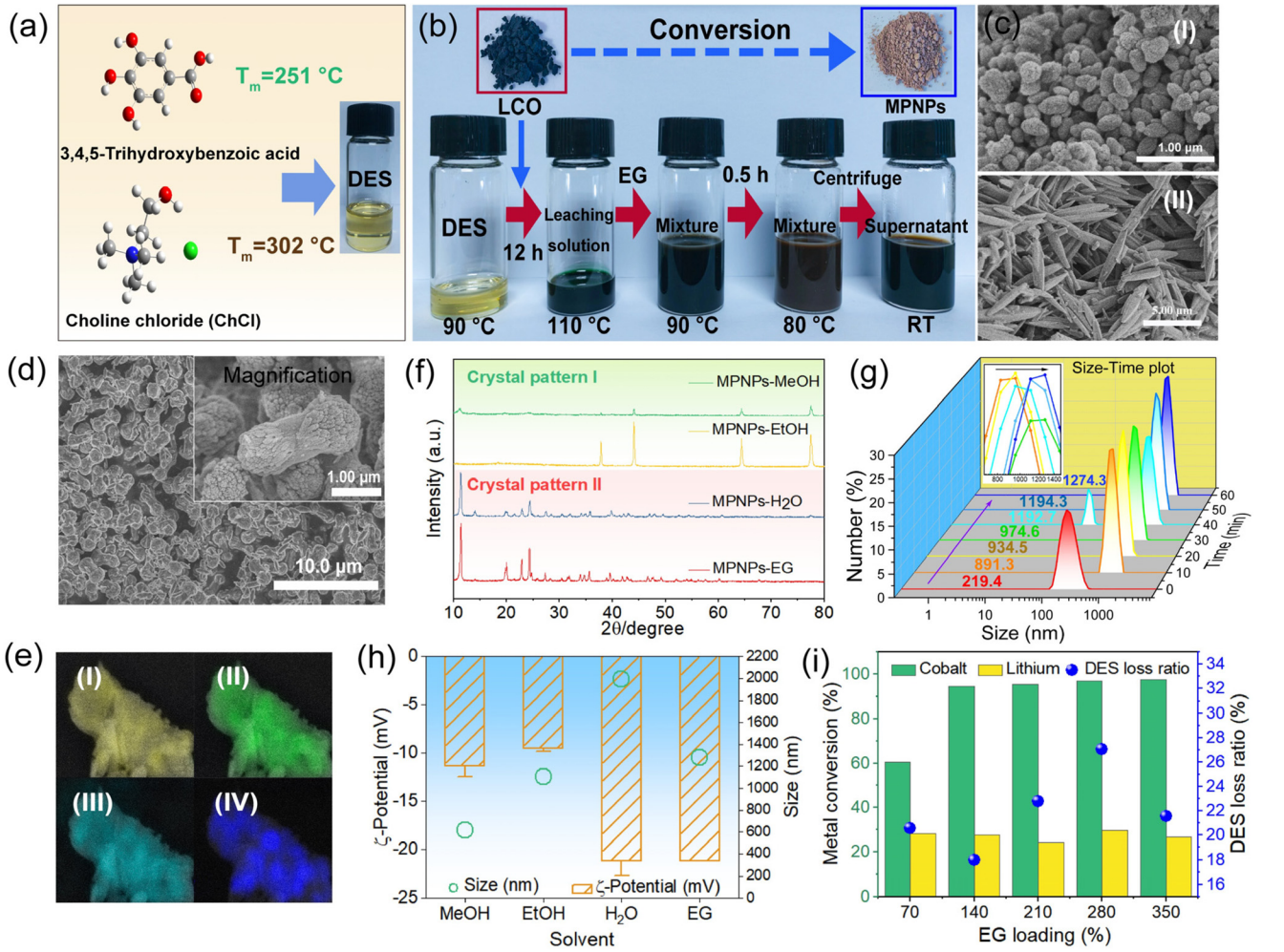

Fig. 1 (a) Composition of DES. (b) Schematic diagram of the solvent-induced self-assembly process. (c) SEM images of MPNPs, utilizing (i) methanol and (ii) H_2O as inducing agents. (d) SEM image of MPNPs, employing EG as an inducer. The inset shows magnified image. (e) EDS elemental mappings of MPNPs: (i) carbon, (ii) oxygen, (iii) cobalt and (iv) chlorine. (f) XRD diagram of MPNPs obtained employing MeOH, EtOH, H_2O and EG respectively. (g) Particle size-number-time change schematic diagram, measured at 10-minute intervals for 60 min following the introduction of EG. The inset displays particle size distribution at different time intervals. (h) Particle size and ζ-potential values of the system after thermostatic heating at 80 °C for 30 minutes. (i) Impact of EG loading (m_{EG}/m_{DES}) on the conversion rate of metal ions.

MPNPs (Fig. S10, ESI†). DES-EG-MPNPs (refer to MPNPs obtained from DES with EG as the inducing agent; other particles named similarly) exhibit a three-stage weight-loss process across the temperature range. When the temperature reaches about 352 °C, the degradation of the aromatic ring, as well as ChCl, occurs. Based on the calculations, the chemical formula of DES-EG-MPNPs was determined to be $Co_3(GA)_2(EG)_3(Ch)_{0.1}Cl_2{\cdot}7H_2O$, while $Co_3(GA)_{2.5}(Ch)_{0.5}Cl_{2.5}(H_2O)_{5.5}{\cdot}3H_2O$ for H_2O and $Co_{2.4}(GA)_{2.6}(Ch)_{1.5}Cl_{2.3}(MeOH)_{3.5}{\cdot}H_2O$ for MeOH. Furthermore, the aromatic ring degradation temperatures in DES-H_2O/MeOH-MPNPs reach 512 °C and 483 °C, respectively, indicating greater stability of MPN structures than DES-EG-MPNPs (T = 352 °C) and GA molecules (T = 274 °C).

We monitored the growth process of MPNPs using dynamic light scattering (DLS). Upon addition of EG, cobalt ions in the solution rapidly form nuclei with ligand molecules, initiating the formation of MPN nanoparticles (Fig. 1g). Through multiple interactions, the nanoparticles agglomerate and continue to grow, reaching a micro-scale. At 40 minutes, 92.7 nm particles were observed, but they disappeared after 10 minutes, indicating that changes in size may be attributed to the agglomeration of small-scale nanoparticles. Further investigation of the particle size and stability of other MPNPs is shown in Fig. 1h. The average size is 615.1 nm, 1106 nm, 1990 nm for MeOH, EtOH, and H_2O respectively. The corresponding ζ-potential values of the system are −11.36 mV, −9.51 mV, −21.16 mV, and −21.20 mV, indicating the overall instability of MPNPs formed in the system with a tendency to coalesce, especially in EtOH.

Optimization of the leaching efficiency and MPNP yield

The conversion process of LCO into MPNPs comprises two distinct steps (Fig. 1b). The initial step involves the dissolution of

LCO in the DES, followed by a second step of solvent-induced MPNP generation. During the first step, we examined the impact of time, temperature, and solid-to-solid ratio on the leaching efficiency of cobalt and lithium ions, respectively. Cobalt and lithium ions reached their maximum extraction rates after 8 hours, at 110 °C, with a solid-to-solid ratio of 15 mg g^{-1} (Fig, S11, ESI†). At this point, the leaching efficiency of LCO is 98.04% (see ESI† for more details). During the second step, we investigated the influence of constant temperature, inducing agent type and quantity, as well as the concentration of GA and Cl^- in the system on the conversion rate of cobalt ions. Among the four inducing agents, EG demonstrates the highest cobalt ion conversion rate, achieving 95.96% (Fig. S12a, ESI†). However, when H_2O is employed, the conversion rate decreases to 54.84%. MeOH and EtOH exhibit even lower rates. This discrepancy arises from the combination of inducer's position in the spectrochemical series and its polarity.[22] Notably, lithium co-precipitates with cobalt. This may stem from the electrostatic interactions between the lithium ion and the benzene ring (Fig. S13, ESI†).[23] These lithium ions can be eliminated through continuous washing of MPNPs. Other factors were also investigated (Fig. 1i and Fig. S12, ESI†); see ESI† for more details. Overall, the maximum conversion rate was achieved using 140% (m_{EG}/m_{DES}) pure EG as the inducing agent.

Mechanism studies

We investigated the mechanism underlying the assembly process induced by EG between Co(II) and GA. Initially, we examined the changes in the coordination environment of Co (II) in DESs following the addition of EG. Anhydrous $CoCl_2$ was used as the cobalt source. It exhibited three absorption peaks at 627, 664, and 693 nm, corresponding to the distinctive absorption of the tetrahedral complex $[CoCl_4]^{2-}$ (Fig. 2a). Upon addition of EG, the intensity decreased, and concurrently, a new absorption peak at 534 nm emerged, corresponding to the octahedral complex $[Co(EG)_6]^{2+}$. This observation confirms the transition of Co(II) from complex anions to cations. Further studies show that the deprotonated GA anion, rather than the neutral molecule, is the object of cation assembly (Fig. S14, ESI†), as the process of ligand deprotonation can significantly accelerate the rate of nucleation.[24] GA anions are primarily derived from GA molecules releasing H^+ ions to bind with lattice oxygen during their reaction with LCO. The assembly kinetics hinge on electrostatic interactions. Prior to the addition of EG, the robust electrostatic repulsion between $[CoCl_4]^{2-}$ and GA anions would hinder the assembly process. UV-vis spectroscopy further reveals the formation of coordination bonds within the MPN (Fig. 2b). In contrast to GA, MPNPs exhibit a broad, rising absorption shoulder peak spanning from 350 nm to 800 nm. This arises from the overlap of polymorphic coordination modes of absorption between metal ions and ligands.[17] The peak at 586 nm corresponds to the ligand-to-metal charge transfer (LMCT) band from GA to metal ions.[25] Disassembled MPNPs display new absorption peaks at 344 nm and 419 nm. These bands are associated with soluble cobalt complex ions resulting from MPN decomposition. Fig. 2c presents the electrospray ionization-mass spectrometry (ESI-MS) anion pattern of disassembled MPNPs. The most prominent signal appeared at m/z = 169.01, corresponding to the $[GA]^-$ anion. In contrast, the signal corresponding to dimerized $[GA_2]^-$ at m/z = 339.03 was relatively low. No discernible signal was detected at higher degrees of polymerization, indicating that the formation of particles is primarily attributed to coordination bonds rather than oxidative polymerization. In the cation mode, the most prominent signal appears at m/z = 104.10, representing $[Ch]^+$ ions (Fig. S15, ESI†). This signal corroborates the formation of coordination bonds between choline cations and Co(II). Raman spectroscopy further reveals the coordination modes between $[GA]^-$ and Co(II). The C═O vibration in the carboxyl group is observed at 1691 cm^{-1} (Fig. 2f). Upon the formation of MPN, the C═O stretching vibration vanishes, and the asymmetric and symmetric stretching vibration of carboxylate (ν_{as} and ν_s) emerges at 1565 cm^{-1} and 1463 cm^{-1}. The difference between them (ν_{as} and $\nu_{s)}$ is 102 cm^{-1}, indicating the type III bridging mode.[21]

X-ray photoelectron spectroscopy (XPS) unveils the alteration in the valence of elemental Co from LCO to MPNPs (Fig. 2e). In LCO, the Co 2p binding energy is observed at 780.13 eV and 795.29 eV, indicative of Co(III). In contrast, in MPNPs, the Co $2p_{3/2}$ binding energy is at 781.45 eV, and $2p_{1/2}$ is at 797.69 eV, corresponding to Co(II). This suggests the reduction of Co(III) in LCO during the leaching process. Similar results are obtained when H_2O is employed as the inducing agent (Fig. S8a, ESI†). Conversely, MPNPs obtained with MeOH and EtOH exhibit a mixed valence state (Fig. S8b, c, ESI†). The disparity in valence, resulting in distinct coordination environments for cobalt ions, could account for both the variations and similarities in the structure of crystalline MPNPs produced by different inducing agents. The tetravalent cobalt may arise from the disproportionation of trivalent cobalt in solutions.[26] To elucidate the reducing agent of Co(III) in the system, we simulated the *in situ* reaction process of DESs with LCO using thermogravimetric-mass spectra (TG-MS) (Fig. 2h). The signal intensities corresponding to mass-to-charge ratios (m/z) of 16, 35, 36, 37 and 38 gradually enhanced over the 2-hour duration, signifying the continuous generation of Cl_2 and O_2 throughout the reaction process. The intensity of the O_2 signal at 10 minutes exhibited a similar pattern to that of the ambient warming process. This can be attributed to the influence of ambient temperature on the reaction of Cl_2 with H_2O, generating O_2. A signal linked to CO_2 (m/z = 44) was also observed, originating from the reduction of organic compound. According to these results, Cl^- serves as the reducing agent of Co(III), and GA may also play a similar role. We further examined the impact of solvation parameters of the system on the yield of MPNPs. The Kamlet–Taft (KT) parameter was employed to assess the solvent characteristics of the system, while Nile red and 4-nitroaniline dye molecules were utilized as probes to ascertain the α, β and π* values.[27] The calculation formulas are provided in ESI.† The conversion rate of Co(II) is graphed against the α value, revealing an "n" curve (Fig. 2g).

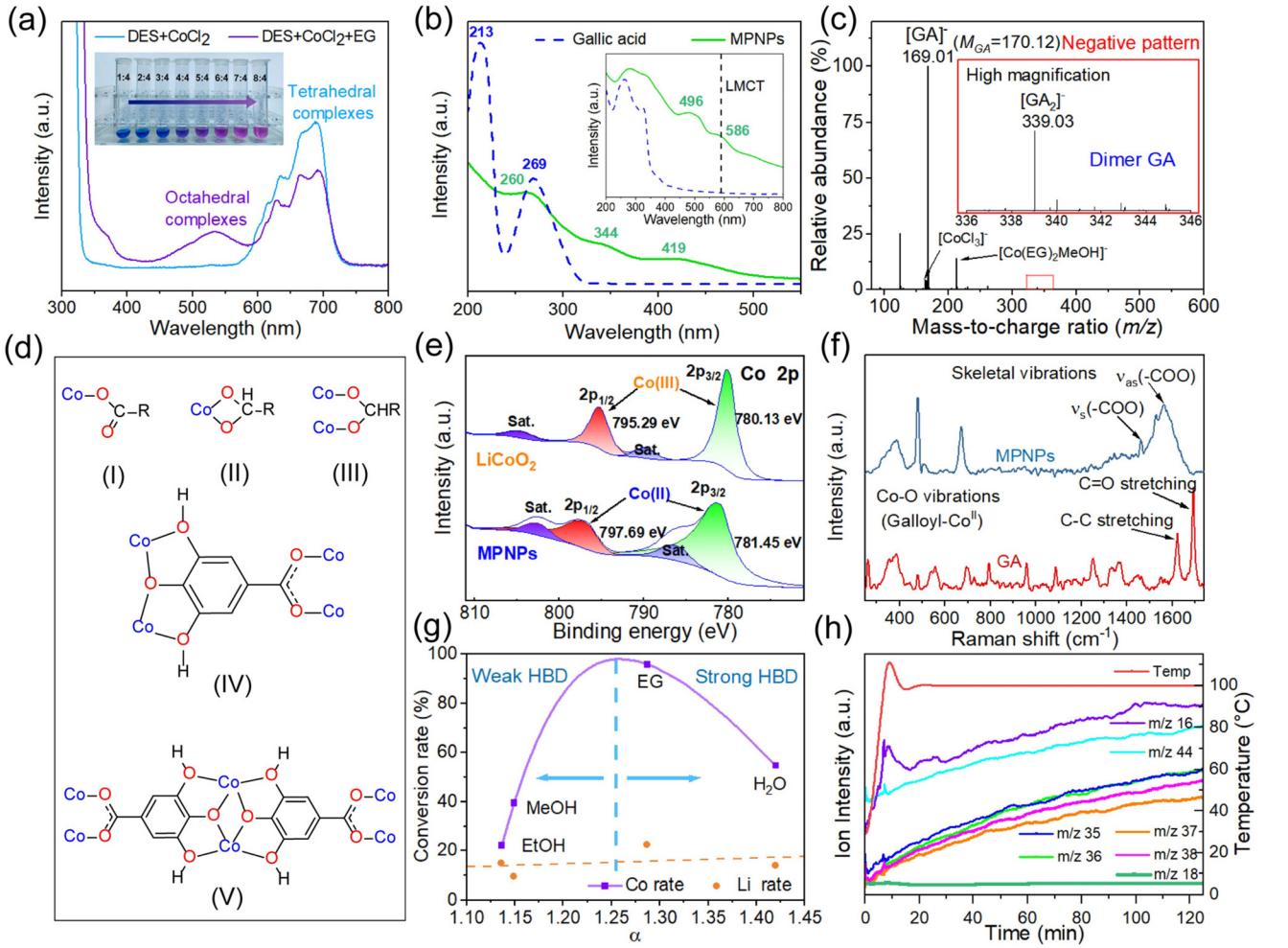

Fig. 2 (a) UV-vis absorption spectra of Co(II) complexes in DES before and after the introduction of EG. The inset displays color variation across the volume ratio ranging from 1 : 4 to 8 : 4 (V_{EG} : V_{DES}). (b) UV-vis absorption spectra of DES-EG-MPNPs after disassembly. The inset exhibits the diffuse reflectance spectra of MPNPs. (c) ESI-MS of DES-EG-MPNPs. Signal at m/z = 169.01 is associated with the $[GA]^-$ anion. (d) Coordination modes of −COOH (upper, i–iii) and galloyl (lower, iv–v) of GA within the MPN.[20] (e) XPS image of cobalt in LCO and DES-EG-MPNPs. (f) Raman spectra of DES-EG-MPNPs. (g) Hydrogen bond acidity (α) of the "DES + inducing agent" system *versus* conversion rate of metal ions. (h) TG-MS plot of the *in situ* simulation of DES-LCO reactions.

This means that low hydrogen bond acidity enhances the conversion process, while high values hinder it. The phenomenon arises because the inducing agent has the propensity to create hydrogen bonds with both Cl^- and $[GA]^-$. The former, serving as the acceptor, diminishes the solvation of $[Co(EG)_6]^{2+}$. Conversely, the latter hampers the assembly process with cobalt ions due to solvation. Therefore, EG stands as the most suitable inducer for MPNP crystallization.

One-step conversion strategy in GA solutions

Building upon the research above, we conducted investigations into the one-step conversion from LCO into MPNPs, in which the dissolution of LCO and the assembly of MPN crystals are achieved in a single step. The EG solution of GA was employed instead of GA-based DESs to achieve this process. A substantial quantity of MPNPs was produced after the reaction, displaying rod-like structures with dimensions on micro-scale (Fig. 3a and Fig. S17a, ESI†). Meanwhile, MPNPs obtained in H_2O, MeOH, and EtOH solutions exhibited leaf-shaped morphology (Fig. S17b, ESI†), rod-shaped morphology (Fig. 3b-i), and irregular agglomerates (Fig. 3b-ii), with dimensions of 9 μm, 3 μm, and 8 μm, respectively.

The impact of Cl^- in the one-step process was also investigated by adjusting the addition of chloride salts in the system. XPS spectra of MPNPs (from MeOH) are presented in Fig. 3c. With the inclusion of LiCl, Co displays mixed valence states within the products, resulting from the incomplete reaction of LCO (Fig. S18a, ESI†). However, the Co(III) signal vanishes after introducing LiCl. The deconvolution of the XPS spectra indicates that the Co(II) and Co(III) contents in products amounted to 19.84% and 80.16% respectively, which turns to 98.91% and 1.09% in the presence of LiCl (Fig. 3d). The disparity highlights the reducing role of Cl^-. It is noteworthy that no difference in MPNPs is observed in EG (Fig. S19, ESI†), resulting

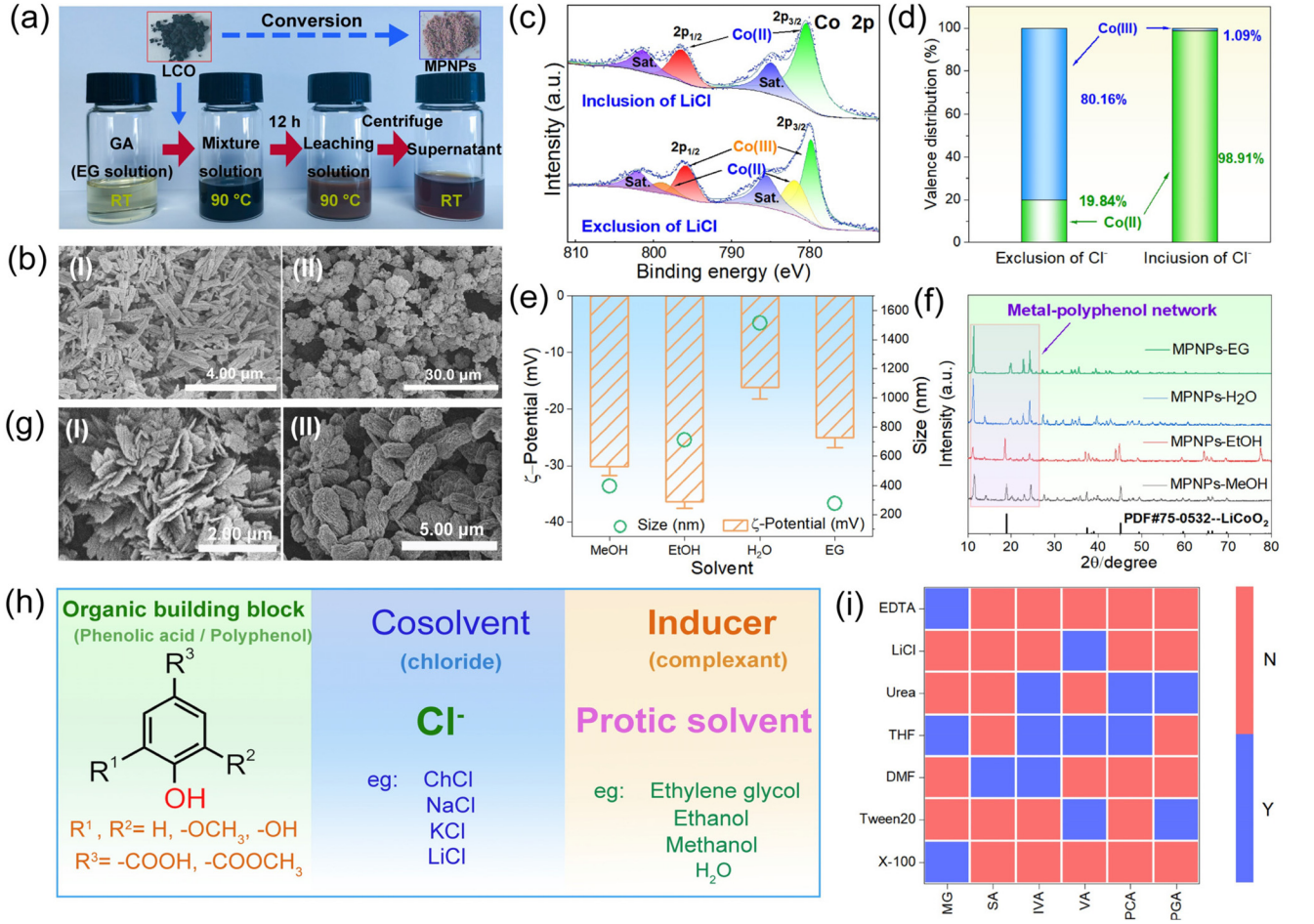

Fig. 3 (a) Schematic diagram of the one-step conversion strategy from LCO to MPNPs. (b) SEM images of MPNPs acquired from (i) MeOH (denoted as GA-MeOH-MPNPs) and (ii) EtOH. (c) XPS image of cobalt in GA-MeOH-MPNPs with the inclusion and exclusion of LiCl. (d) Relative content of Co (III) and Co(II) in products of MeOH solution, with the system inclusion and exclusion of LiCl. (e) Particle size and ζ-potential values of systems after 12-hour reaction with LCO employing different dispersants, along with the introduction of LiCl as the Cl^- source. (f) XRD diagram of MPNPs obtained by the one-step conversion strategy. The observation of fine diffraction peaks signifies the crystalline nature of MPNPs. (g) SEM images of MPNPs acquired from two systems: (i) isovanillic acid-EG-LiCl and (ii) gallate-EG-LiCl. (h) General formula of the proposed system for achieving the one-step conversion strategy. (i) Stability of MPNPs obtained from the "polyphenol derivatives-EG-LiCl" system in the presence of different competitive agents. Instability was indicated by red, while stability was denoted by blue.

from the reducing capacity of EG.[28] Further research demonstrates that the content of Cl^- significantly impacts the generation kinetics of MPNPs. We roughly quantified the disparity in reaction kinetics by measuring the apparent generation time t and monitoring the reaction process by XRD. t is defined as the critical reaction time for the color change of the solution, signifying the generation of a substantial quantity of MPNPs. The results indicate that a low concentration of Cl^- promotes the conversion process and *vice versa* (Fig. S21, ESI†). Experiments are also conducted in solutions of MeOH, H_2O, and EtOH (Fig. S22, ESI†). XRD analysis corroborates the facilitating action of Cl^- on the conversion rate of MPNPs (Fig. S23, ESI†). It was observed that an escalation in Cl^- loading corresponded to the augmented conversion rate in both EG and MeOH solutions. In contrast, the EtOH solution showed no presence of MPNPs, whereas the H_2O solution exhibited complete conversion. Consequently, the relative rates are ordered hierarchically as follows: EtOH < MeOH, EG < H_2O. Additionally, Cl^- influences the size of MPNPs. With the inclusion of LiCl, the average particle sizes are as follows: 396.1 nm (MeOH), 712.4 nm (EtOH), 1515.3 nm (H_2O), and 277.7 nm (EG) (Fig. 3e), resulting in a notable reduction in the presence of LiCl (Fig. 3b and Fig. S17, ESI†). Simultaneously, the ζ-potential values are as follows: −30.1 mV (MeOH), −36.4 mV (EtOH), −16.2 mV (H_2O), and −25.06 mV (EG), indicating stability in both MeOH and EtOH environments.

Through disassembly experiments on MPNPs, we were able to ascertain the production of quinones resulting from the oxidation of GA (Fig. S24, ESI†). FT-IR spectra provide insights into the structural similarities between MPNPs obtained *via* both one-step and two-step methods (Fig. S26, ESI†).

Generalized system for the strategy

Drawing from our findings, we propose a generalized system for the one-step conversion strategy of LCO into MPNPs (Fig. 3h). The system comprises three fundamental components: an organic building block, a co-solvent, and an inducing agent. The organic building blocks commonly encompass phenolic acids, polyphenolic compounds, and their derivatives, distinguished by the presence of oxygen-containing functional groups arranged in non-neighboring positions. The co-solvents primarily consist of chloride salts, including LiCl, ChCl, and others. They facilitate the dissolution of LCO through the redox process. Inducing agents typically include EG, MeOH, EtOH, and H_2O. They function as ligand-exchange inducers, effectively promoting the assembly of MPN crystals. Notably, Cl^- is not an absolute requirement, as polyphenols inherently possess reducing capabilities. Nevertheless, the inclusion of Cl^- accelerates the conversion process into MPNPs.

Experiments with other six polyphenol derivatives were conducted. Fig. S27a† displays the suspensions resulting from the reactions of these polyphenol derivatives. The obtained MPNPs are visualized in Fig. S27b.† SEM images reveal that isovanillic acid (IVA)-Co exhibits a lamellar structure, with a dimension of 1.8 μm in size and 100 nanometer in thickness (Fig. 3g–i). Methyl gallate (MG)-Co displays a unique "peanut" structure, measuring 1.6 μm in size. Other SEM images are presented in Fig. S28.† To gain a deeper understanding of the stabilizing interactions of these MPNPs, we conducted a comprehensive investigation involving the use of various competitive agents.[17] The results are presented in Fig. 3i. These observations highlight the pivotal roles played by metal coordination and hydrophobic interactions in the stabilization of MPNPs.

Strategy applied in LCO recovery and regeneration

Based on the studies conducted in GA-based DES and GA solutions, we proposed the mechanistic diagram illustrating the solvent-induced conversion process from LCO into MPNPs (Fig. 4a). Initially, a portion of GA molecules within the solution will adsorb onto the surface of LCO due to physical interactions. These molecules will facilitate the release of metal ions into the solution through the rupture of the M–O bond.

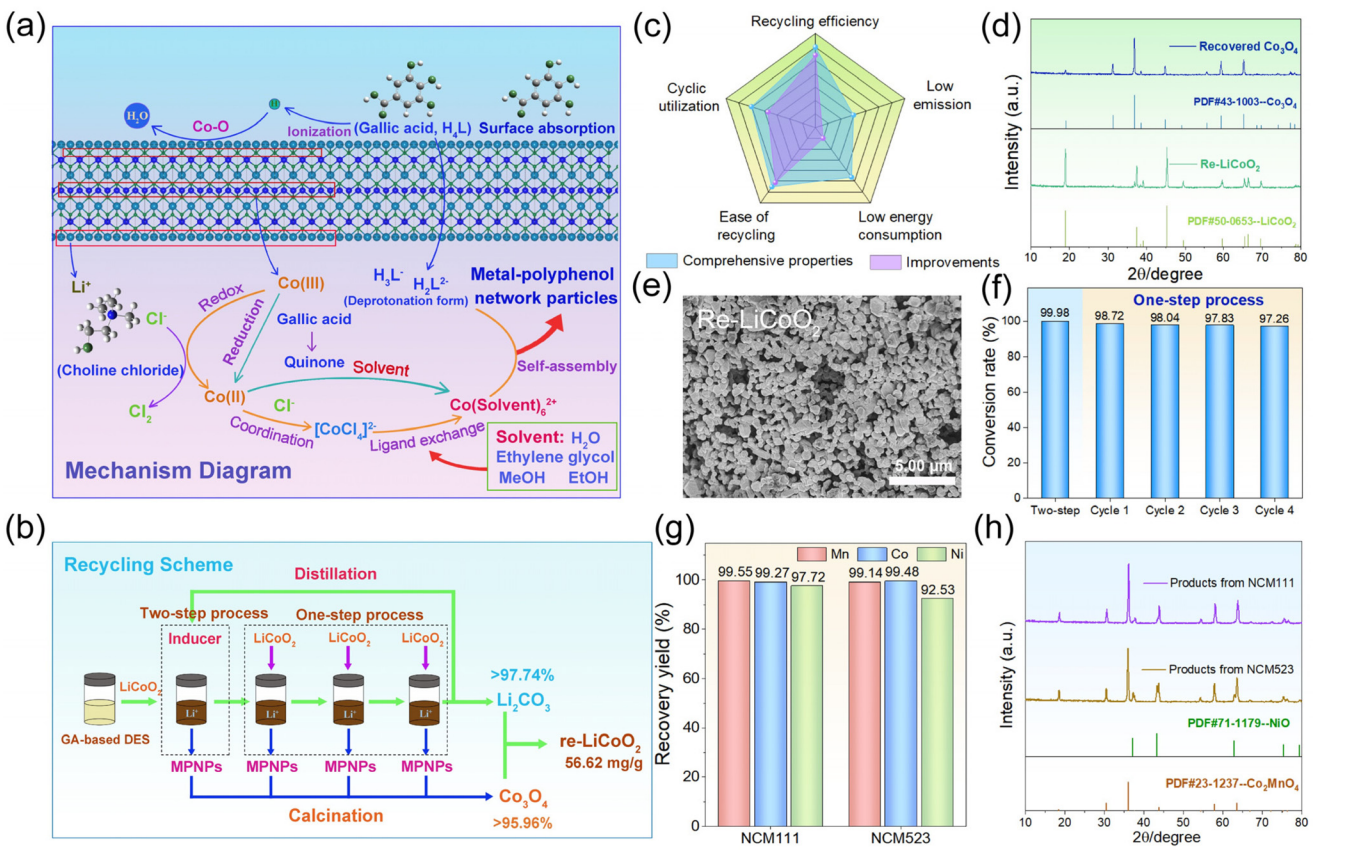

Fig. 4 (a) Proposed mechanistic diagram of the solvent-induced self-assembly process from LCO into MPNPs, encompassing the two-step (orange line) and one-step (green line) strategies. (b) Scheme of SIC method utilized for recycling and regeneration of LCO. (c) Simulated radar diagram of the recycling scheme. The blue region signifies the comprehensive properties, while the purple area denotes the aspects of improvement. (d) XRD diagram of Recovered-Co_3O_4 and Re-$LiCoO_2$. (e) SEM image of the regenerated LCO. (f) Conversion rate of dissolved cobalt ions to MPNPs. The yellow area represents the continuous addition of LCO during the one-step process. (g) Recovery yield of metal ions from NCM111 and NCM523 through the scheme. (h) XRD diagram of the calcined products of MPNPs obtained employing NCM111 and NCM523 as metal sources.

Simultaneously, they will undergo transformation into deprotonated forms. The released Co(III) ions will undergo reduction to Co(II) and form the $[CoCl_4]^{2-}$ complex in the presence of Cl^-, which concurrently undergo oxidation to yield Cl_2. At this juncture, the inducing agents, with their superior metal ion binding capacities, will facilitate the conversion of $[CoCl_4]^{2-}$ into $[Co(Solvent)_6]^{2+}$ *via* ligand exchange, altering the electrical characteristics of the complex. The formed complex will utilize interionic electrostatic forces to associate with $[GA]^-$ species, forming MPN coordination polymers that will crystallize within the system owing to low solubility properties. In the absence of Cl^-, GA molecules donate electrons to reduce Co(III) while undergoing oxidation to quinone.

We propose a spent LCO battery recycling scheme based on SIC, illustrated in Fig. 4b, and the disassembly process of batteries is shown in Fig. S29.† The recycling process begins with the dissolution of LCO in the GA-based DES, followed by the addition of EG. This step is essential for facilitating the conversion of cobalt ions into insoluble MPN crystal particles, which subsequently separate from solution. The simultaneous presence of GA, Cl^- and EG in the system post-reaction allows for the attainment of one-step conversion process to produce MPNPs. At each step, the MPNPs undergo purification, which involves the removal of surface-adsorbed lithium ions *via* a washing process, ultimately yielding Co_3O_4 *via* high-temperature calcination. XRD analysis confirms the successful formation of Co_3O_4, with no detection of impurity peaks related to Li_2CO_3 (Fig. 4d). SEM image reveals that the recovered Co_3O_4 exhibits an irregular bulk structure (Fig. S31, ESI†). Lithium ions progressively accumulate in the solution throughout the entire process. After undergoing four one-step conversions, the residual solution is subjected to calcination to produce Li_2CO_3. Subsequently, it is combined with Co_3O_4 through grinding and calcination, while maintaining a Li/Co molar ratio of 1.05 : 1 to produce regenerated $LiCoO_2$, referred to as re-$LiCoO_2$. XRD diagram demonstrates the successful regeneration of LCO (Fig. 4d). It exhibits a typical layered α-$NaFeO_2$ structure, which is consistent with the $LiCoO_2$ standard PDF card (PDF#50-0653). SEM image reveals the appearance of re-$LiCoO_2$ (Fig. 4e). When MeOH and EtOH are utilized as inducing agents, they can be separated from the system through distillation and subsequently reused during the "two-step process". Fig. S32† illustrates the successful regeneration of these inducing agents. The conversion rate of cobalt ions to MPNPs at each step is shown in Fig. 4f. Through calculation, the recycling scheme can achieve a $LiCoO_2$ regeneration rate of 56.62 mg g^{-1} of DES, emphasizing regeneration over dissolution. Fig. 4c depicts the simulated evaluation of this scheme. The blue region showcases the comprehensive properties of the scheme. In contrast to other works, our scheme exhibits enhancements in recycling efficiency, recyclability, and ease of recycling (purple region).[29–31] We also explored the applicability of the scheme. When NCM111 and NCM523 served as metal sources, over 97.72% and 92.53% of metal ions could be recovered, respectively (Fig. 4g). Fig. 4h illustrates the oxide precursor of MPNP post-calcination, wherein cobalt and manganese are retrieved as Co_2MnO_4 and nickel as NiO. These results underscore the widespread applicability of our scheme to diverse electrode materials. The distinctive network structure of MPNPs holds promise for trapping dye molecules and heavy metal ions in water. We will publish details related to this in a separate work in the future.

Conclusions

We have successfully achieved the conversion process, wherein the spent $LiCoO_2$ cathode materials have been transformed into crystalline cobalt-based MPNPs using GA-based DESs *via* solvent-induced crystallization. The process involves two steps: dissolution and crystallization. We discovered that EG, H_2O, MeOH, and EtOH are effective inducing agents for producing crystalline MPNPs. The conversion efficiency is correlated with the inducer's position in the spectrochemical series and its hydrogen bonding acidity (α). XRD and XPS analyses revealed that the crystal structure of MPNPs was influenced by the valence of the cobalt ion and its coordination environment, which was associated with the inducer. Moreover, we achieved the afore-mentioned conversion process in GA-based solutions in a single step. Comprehensive investigations revealed that efficient transformation can be achieved when the system incorporates organic building blocks, inducing agents, and Cl^-. Based on these results, we devised a tandem recycling scheme for the spent $LiCoO_2$ materials, in which the obtained MPNPs were further converted into Co_3O_4 precursors by calcination and regenerated $LiCoO_2$ with the obtained Li_2CO_3. The experimental results for ternary electrode materials demonstrated that our scheme can recycle over 97.72% of transition metals, signifying its robust generalizability.

Author contributions

Zeyu Wang: investigation, writing – original draft, and writing – review & editing. Rui Qin, Fengyi Zhou, Yurun Tian: investigation. Yu Chen, Zhimin Xue: conceptualization, and writing – review & editing. Tiancheng Mu: conceptualization, writing – review & editing, and supervision.

Conflicts of interest

There are no conflicts to declare.

Acknowledgements

The authors thank the National Natural Science Foundation of China (22238011, 22073112) for financial support.

References

1 E. Pomerantseva, F. Bonaccorso, X. Feng, Y. Cui and Y. Gogotsi, *Science*, 2019, **366**, eaan8285.
2 J. Wu, A. Mackenzie and N. Sharma, *Green Chem.*, 2020, **22**, 2244–2254.
3 J. Kumar, R. R. Neiber, J. Park, R. Ali Soomro, G. W. Greene, S. Ali Mazari, H. Young Seo, J. Hong Lee, M. Shon, D. Wook Chang and K. Yong Cho, *Chem. Eng. J.*, 2022, **431**, 133993.
4 J. Xiao, F. Shi, T. Glossmann, C. Burnett and Z. Liu, *Nat. Energy*, 2023, **8**, 329–339.
5 X. Chang, M. Fan, C. Gu, W. He, Q. Meng, L. Wan and Y. Guo, *Angew. Chem., Int. Ed.*, 2022, **61**, e202202558.
6 G. Harper, R. Sommerville, E. Kendrick, L. Driscoll, P. Slater, R. Stolkin, A. Walton, P. Christensen, O. Heidrich, S. Lambert, A. Abbott, K. Ryder, L. Gaines and P. Anderson, *Nature*, 2019, **575**, 75–86.
7 M. K. Tran, M.-T. F. Rodrigues, K. Kato, G. Babu and P. M. Ajayan, *Nat. Energy*, 2019, **4**, 339–345.
8 D. Yu, Z. Xue and T. Mu, *Chem. Soc. Rev.*, 2021, **50**, 8596–8638.
9 S. H. Alhashim, S. Bhattacharyya, R. Tromer, A. Kabbani, G. Babu, E. F. Oliveira, D. S. Galvao and P. M. Ajayan, *ACS Sustainable Chem. Eng.*, 2023, **11**, 6914–6922.
10 R. Morina, D. Callegari, D. Merli, G. Alberti, P. Mustarelli and E. Quartarone, *ChemSusChem*, 2022, **15**, e202102080.
11 N. Peeters, K. Binnemans and S. Riaño, *Green Chem.*, 2020, **22**, 4210–4221.
12 C. Ma, M. Svärd and K. Forsberg, *Resour., Conserv. Recycl.*, 2022, **186**, 106579.
13 Y. Hua, Y. Sun, F. Yan, S. Wang, Z. Xu, B. Zhao and Z. Zhang, *Chem. Eng. J.*, 2022, **436**, 133200.
14 M. Oh and C. A. Mirkin, *Nature*, 2005, **438**, 651–654.
15 J. Guo, Y. Ping, H. Ejima, K. Alt, M. Meissner, J. J. Richardson, Y. Yan, K. Peter, D. von Elverfeldt, C. E. Hagemeyer and F. Caruso, *Angew. Chem., Int. Ed.*, 2014, **53**, 5546–5551.
16 H. Ejima, J. J. Richardson, K. Liang, J. P. Best, M. P. Van Koeverden, G. K. Such, J. Cui and F. Caruso, *Science*, 2013, **341**, 154–157.
17 W. Xu, Z. Lin, S. Pan, J. Chen, T. Wang, C. Cortez-Jugo and F. Caruso, *Angew. Chem., Int. Ed.*, 2023, **62**, e202312925.
18 M. Oh and C. A. Mirkin, *Angew. Chem., Int. Ed.*, 2006, **45**, 5492–5494.
19 S. Wang, Z. Zhang, Z. Lu and Z. Xu, *Green Chem.*, 2020, **22**, 4473–4482.
20 Md. A. Rahim, K. Kempe, M. Müllner, H. Ejima, Y. Ju, M. P. Van Koeverden, T. Suma, J. A. Braunger, M. G. Leeming, B. F. Abrahams and F. Caruso, *Chem. Mater.*, 2015, **27**, 5825–5832.
21 R. K. Feller and A. K. Cheetham, *Solid State Sci.*, 2006, **8**, 1121–1125.
22 D. Knetsch and W. L. Groeneveld, *Recl. Trav. Chim. Pays-Bas*, 1973, **92**, 855–864.
23 P. Wang, X. Lou, C. Li, X. Hu, Q. Yang and B. Hu, *Nano-Micro Lett.*, 2018, **10**, 19.
24 W. J. Rieter, K. M. Pott, K. M. L. Taylor and W. Lin, *J. Am. Chem. Soc.*, 2008, **130**, 11584–11585.
25 Md. A. Rahim, M. Björnmalm, N. Bertleff-Zieschang, Q. Besford, S. Mettu, T. Suma, M. Faria and F. Caruso, *Adv. Mater.*, 2017, **29**, 1606717.
26 R. Gupta and A. Manthiram, *J. Solid State Chem.*, 1996, **121**, 483–491.
27 H. Yu, Z. Xue, X. Lan, Q. Liu, R. Shi and T. Mu, *Cellulose*, 2020, **27**, 6175–6188.
28 T. Matsumoto, K. Takahashi, K. Kitagishi, K. Shinoda, J. L. Cuya Huaman, J.-Y. Piquemal and B. Jeyadevan, *New J. Chem.*, 2015, **39**, 5008–5018.
29 T. Hu, T. Li, X. Liu, Z. Wang, L. Lou, S. Jing, X. Yan, Y. Xiong, J. Xiong and X. Ge, *Green Chem.*, 2024, **26**, 2653–2660.
30 T. Li, Y. Xiong, X. Yan, T. Hu, S. Jing, Z. Wang and X. Ge, *J. Energy Chem.*, 2022, **72**, 532–538.
31 L. Lou, X. Liu, Y. Wang, T. Hu, Z. Wang, H. Shi, J. Xiong, S. Jing, L. Ye, Q. Guo and X. Ge, *Chin. Chem. Lett.*, 2024, 109726.

